JACS
JOURNAL OF THE AMERICAN CHEMICAL SOCIETY
Article
pubs.acs.org/JACS

Synergistic Oxygen Evolving Activity of a TiO_2-Rich Reconstructed $SrTiO_3(001)$ Surface

John Mark P. Martirez,[†,§] Seungchul Kim,[†,§,∥] Erie H. Morales,[‡] Benjamin T. Diroll,[§] Matteo Cargnello,[§] Thomas R. Gordon,[§] Christopher B. Murray,[§,‡] Dawn A. Bonnell,[‡] and Andrew M. Rappe*[,†,‡,§]

[†]The Makineni Theoretical Laboratories, Department of Chemistry and [§]Department of Chemistry, University of Pennsylvania, Philadelphia, Pennsylvania 19104−6323 United States

[‡]Department of Materials Science and Engineering, University of Pennsylvania, Philadelphia, Pennsylvania 19104−6202 United States

[∥]Center for Computational Science, Korea Institute of Science and Technology, Seoul 136-791, Republic of Korea

Supporting Information

ABSTRACT: In addition to composition, the structure of a catalyst is another fundamental determinant of its catalytic reactivity. Recently, anomalous Ti oxide-rich surface phases of ternary oxides have been stabilized as nonstoichiometric epitaxial overlayers. These structures give rise to different modes of oxygen binding, which may lead to different oxidative chemistry. Through density functional theory investigations and electrochemical measurements, we predict and subsequently show that such a TiO_2 double-layer surface reconstruction enhances the oxygen evolving activity of the perovskite-type oxide $SrTiO_3$. Our theoretical work suggests that the improved activity of the restructured $TiO_2(001)$ surface toward oxygen formation stems from (i) having two Ti sites with distinct oxidation activity and (ii) being able to form a strong O−O moiety (which reduces overbonding at Ti sites), which is a direct consequence of (iii) having a labile lattice O that is able to directly participate in the reaction. Here, we demonstrate the improvement of the catalytic performance of a well-known and well-studied oxide catalyst through more modern methods of materials processing, predicted through first-principles theoretical modeling.

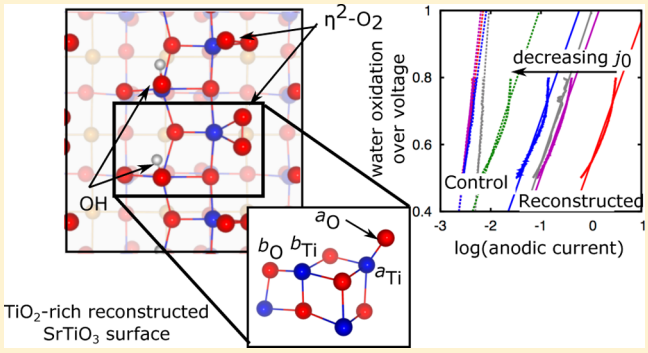

1. INTRODUCTION

Transition-metal-based oxides attract significant attention for their ability to catalyze the highly complex four-electron oxidation of water to molecular oxygen, the pair reaction of water reduction to hydrogen gas.[1] Current works in the field seek the elusive water oxidation catalyst that is effective while only using earth abundant elements. Recent research has focused on a few well-studied transition metals, such as Mn, Fe, Co and Ni, incorporating new synthetic techniques and/or crystallographic structures.[2−9] Through synthetic variations, they have observed different catalytic activities for compositionally similar compounds.

The ability of $SrTiO_3$ to photocatalyze water splitting to generate both H_2 and O_2 upon illumination of ultraviolet light has been known for over three decades.[10−12] Unfortunately, as a photoanode, it cannot absorb light with photon energy less than its large band gap energy of 3.2 eV (UV range).[10,11] This makes it undesirable in photochemical solar energy conversion, since the UV range is only 9% of the solar energy output. It has also been reported that Ti-based oxides, such as $SrTiO_3$, are expected to perform poorly as water oxidation catalysts because Ti^{IV}−O is extremely stable and therefore difficult to activate[13] and that Ti^{IV} is unable to be further oxidized to Ti^{V}, which is in principle required to gather enough oxidizing equivalents to oxidize H_2O to O_2. The photogenerated hole is therefore the key source of its reactivity. Much of the effort toward improving the performance of Ti^{IV} oxides is put into reducing their band gaps via doping, to provide satisfactory absorption closer to or within the visible light range.[14−18] Concurrently, significant work has also been dedicated to studying surface structural modification on perovskite-type oxides, $SrTiO_3$ being one of the most studied, leading to discovery of diverse and chemically distinct surface structures.[19−32]

Recently, anomalous Ti oxide-rich surface phases of ternary oxides have been stabilized as nonstoichiometric epitaxial overlayers with units exhibiting cubane-like motifs.[22−25,27−30] Through an *ab initio* investigation, we predict the enhancement of the oxygen evolving activity of $SrTiO_3$, via the aforementioned surface structure modification, and we confirm the enhancement through electrochemical measurements. Interestingly, the reconstruction presents a diversity of Ti-O bonding environments, where some bonds are more covalent than others. This makes some surface Ti ions more electron-rich

Received: November 4, 2014
Published: February 9, 2015

DOI: 10.1021/ja511332y
J. Am. Chem. Soc. 2015, 137, 2939−2947

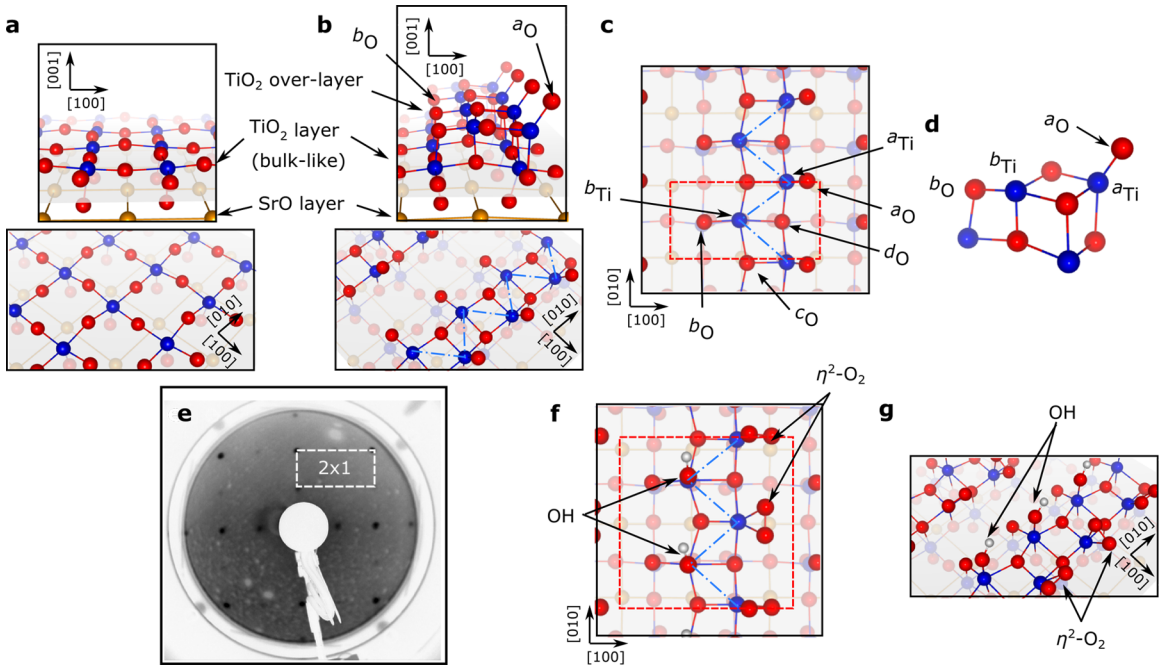

Figure 1. Structure of the $SrTiO_3(001)$ bulk-like and DL reconstructed surfaces. (a) The bulk-like TiO_2 and (b) the 2 × 1-DL surfaces.[22] (c) Top-down view of the 2 × 1-DL surface, which shows the surface Ti arranged in a zigzag pattern (traced by the blue dot-dashed line). The 2 × 1 supercell is marked by the red dashed line. (d) Ti_4O_6 subunit of the surface reconstruction exhibiting cubane-like structure. (e) A typical LEED pattern of a double-domain 2 × 1 reconstruction measured at 38 eV, a 2 × 1 pattern is marked. (f) Highly oxidized derivative of the 2 × 1-DL, predicted to be stable under catalytic conditions (B5 in Figure 3, R4 in Figure 4b). The 2 × 2 supercell simulation size is marked by the red dashed lines. (g) Angled view of the structure in (f).

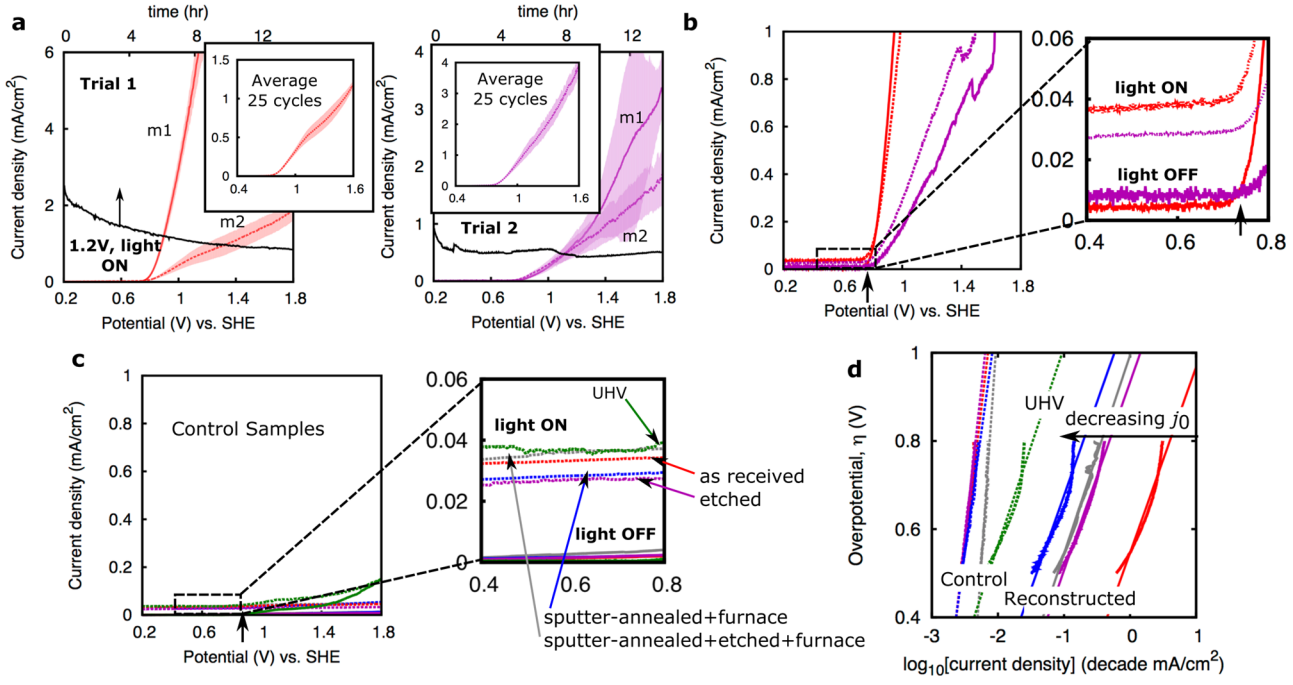

Figure 2. (a) *I*−*V* (vs standard hydrogen electrode, SHE, at 10 mV/s, average of five anodic−cathodic scan cycles), colored lines, and *I*−*t* (at 1.2 V vs SHE with UV−vis illumination), black lines, plots for the surface reconstructed samples. Shaded regions correspond to the current standard deviation and surface area uncertainty. m1 and m2 denote measurements from fresh samples and after the 14 h constant voltage electrolysis, respectively. Insets show m2-type measurement averaged over 25 anodic−cathodic scan cycles at 10 mV/s. (b) and (c) *I*−*V* for reconstructed and control samples (1 mV/s, averaged over 2 anodic−cathodic scan cycles), respectively, with and without illumination. Thick arrows mark the onset voltages (≈0.75 V). (d) Tafel plots with linear regression lines. *I*−*V* curves were taken from 1 mV/s data acquisition (averaged over 2 cycles) from 0.9 to 1.2 V vs SHE (η = 0.5−0.8 V). Solid line, surface reconstructed samples; broken line, control. The colors correspond to the same sample color designations in a and c and Figure S1 in the Supporting Information. Tafel parameters are summarized in Table S2 in the Supporting Information.

DOI: 10.1021/ja511332y
J. Am. Chem. Soc. 2015, 137, 2939−2947

than others.[22,24] As we will show, Ti atoms with different bonding environments on a nonstoichiometric surface show novel catalytic behavior; they can interact differently with O species and function as a single catalytic unit by playing complementary roles in the reaction, thereby improving the energetics of the four-step water oxidation. Our work suggests that a crucial aspect for the catalytic synthesis of dioxygen on this surface is the cooperative work between an oxidizable active site that can accommodate electrophillic O species and a weak Lewis acid site that acts a repository of nucleophilic O species. Furthermore, these two sites must be in electronic communication with each other.

$SrTiO_3$, a perovskite-type oxide, has alternating layers of SrO and TiO_2 along its [001] crystallographic axis. Figure 1a shows the TiO_2 exposed (001) termination with the corner-shared square planar TiO_4 units on the surface layer. It has been reported that a TiO_2-rich surface reconstruction forms when the $SrTiO_3$ (001) surface is heated to 900−1100 °C and exposed to a continuous flow of O_2, after aggressive Ar^+ sputtering,[22−25] although other synthetic methods and conditions have found similar surface reconstructions.[19,21,29] These reconstructions are generally found to be composed of a bulk-like TiO_2 layer supporting a TiO_2 overlayer or collectively a double-layer (DL).[22−25,27−30] The 2 × 1 TiO_2-DL reconstruction (Figure 1b) has an overlayer composed of edge-shared TiO_4 units distributed in a zigzag ladder pattern, and each overlayer Ti sits atop a surface oxygen.[22,24,33−36] The laterally unshared O atoms are either one- or two-fold coordinated, ^{a}O and ^{b}O, respectively, while the laterally shared O atoms are either three- or four-fold coordinated, ^{c}O and ^{d}O, respectively (^{b}O and ^{d}O sit atop subsurface layer Ti), see Figure 1c). The bonding between overlayer ^{a}Ti and ^{a}O is quite covalent, since O is divalent and ^{a}O is singly coordinated. Figure 1d shows the cubane-like Ti_4O_6 subunit of the surface.

The exceptional stability of this reconstruction under oxidizing conditions[23] and its diverse Ti-O bonding character and O coordination number[22] prompt us to evaluate these surfaces (such as the 2 × 1-DL) as potential catalysts for oxidative chemistry.

2. RESULTS AND DISCUSSION

2.1. Photoelectrochemical Measurements. Four 2 × 1 surface reconstructed Nb-doped (1.4 mol %) $SrTiO_3$ single crystals were prepared, and the appearance of the reconstruction was confirmed via low-energy electron diffraction (LEED), as shown in Figure 1e. Heavily doped samples were chosen to decouple variation in the bulk conductivity from surface reconstruction due to processing. Indeed, resistivity measurements indicate that none of the processing required to create the reconstruction significantly alters the bulk electrical properties (see Table S1 in the Supporting Information). Photoelectrochemical measurements were performed on these reconstructed samples. Figure 2a shows the current vs voltage (I−V) curves of the surface reconstructed samples (see also Figure S1 in the Supporting Information) with onset voltages of ≈0.75 V vs the standard hydrogen electrode (SHE). Along with the I−V curves, the current vs time (I-t) curves (black lines), at constant potential and UV−vis illumination, are plotted. Stable current densities of about 0.1−1 mA cm^{-2} at 1.2 V were obtained corresponding to turnover numbers of ≈1−10 $\mu molO_2$ hr^{-1} cm^{-2} assuming Faradaic efficiency of unity. The contribution of the photoexcitation to the catalytic activity in all cases is found to be minimal (≈0.02−0.04 mA/cm^2 shift in the current density at low potentials), Figure 2b; this is as expected for heavily doped semiconductors, where the free carriers effectively screen or reflect incident photons. It was previously demonstrated that the photocurrent measured under anodic bias may decrease 3-fold when going from 0.07% to 0.69% mol % Nb under UV illumination.[16] Ellipsometric measurements show that the optical properties of the samples are unperturbed by their history (see Figure S2 in the Supporting Information). I−V curves for control samples (with no reconstruction) with and without UV−vis illumination were also obtained, Figure 2c. Much lower current densities were obtained from these samples and they are at least an order of magnitude less than the surface-reconstructed samples at potentials greater than 0.9 V.

The anodic current density, j, is known to increase exponentially with overpotential, the difference between the applied potential, U, and the equilibrium reduction potential, ε_{eq} = 0.40 V vs SHE at pH = 14. This is expressed in the Tafel relation: $j = j_o \exp(\eta/A)$, where j_o is the exchange current density and A is the temperature-dependent Tafel slope.[37] η is usually plotted against $\log_{10}(j)$, $\eta = 2.303A \log(j/j_o)$ which are shown in Figure 2d.[37] Tafel slopes ≈0.20 V with exchange current densities of 0.003−0.05 mA/cm^2 (see Table S2 in the Supporting Information) were obtained from the reconstructed samples at 0.9−1.2 V potential window. Much higher Tafel slopes (0.5−1 V) and lower exchange current densities (0.001−0.003 mA/cm^2) were found for the control samples, although the UHV annealed sample showed a better Tafel slope (0.20 V) but much lower j_o (0.0006 mA/cm^2). Exclusively annealing $SrTiO_3$ in UHV had been previously shown to produce the 2 × 1 reconstruction,[21] however the surface Ti-enrichment processes[31,38] (sputtering and chemical etching) and calcination in furnace in O_2 are essential for producing very sharp LEED images (indicating large areas of the reconstruction). Thus, the observed enhancement of slope for the UHV annealed control sample is likely due to some surface reconstruction that is undetectable in LEED. Samples exhibiting similar Tafel slopes likely indicate similar catalytic mechanisms; however varying the effective catalytic surface area will lead to changes in their j_o.

In all cases, the activity is observed over prolonged period of time which eventually decreases (compare curves m1 and m2 in Figure 2a), presumably due to the loss in the long-range order at the surface, because of, for example, undesirable adsorbates and the loss of the active surface structure. However, the enhancement of used samples is noticeably better than controls, and simply reannealing them in UHV recovers the catalytic activity. LEED patterns of reannealed samples confirm the existence of 2 × 1 reconstruction indicating that recovering procedure in UHV restores the long-range surface order (see Figures S4−S6 in Supporting Information.)

We have found that this enhancement may be ascribed to the acquired efficiency due to the reconstruction, which enables thermodynamically balanced chemical routes. This is discussed in the following sections.

2.2. Computational Framework. A theoretical framework adapted from refs 39−43 is used to evaluate the surface's oxygen evolving activity through a density functional theory (DFT) thermodynamics approach. The method uses a metric that relies on finding the largest thermodynamic barrier associated with the elementary steps after breaking the reaction: $2H_2O \rightarrow O_2 + 4H^+ + 4e^-$ down into four proton-coupled electron-transfer steps, with appropriate intermediates. For a reaction consisting of four single-electron steps (as in the reaction above): $\eta = U - \varepsilon_{eq} = 1/4 \sum_i^4 [U - \varepsilon(i)]$, where $\varepsilon(i)$

DOI: 10.1021/ja511332y
J. Am. Chem. Soc. 2015, 137, 2939−2947

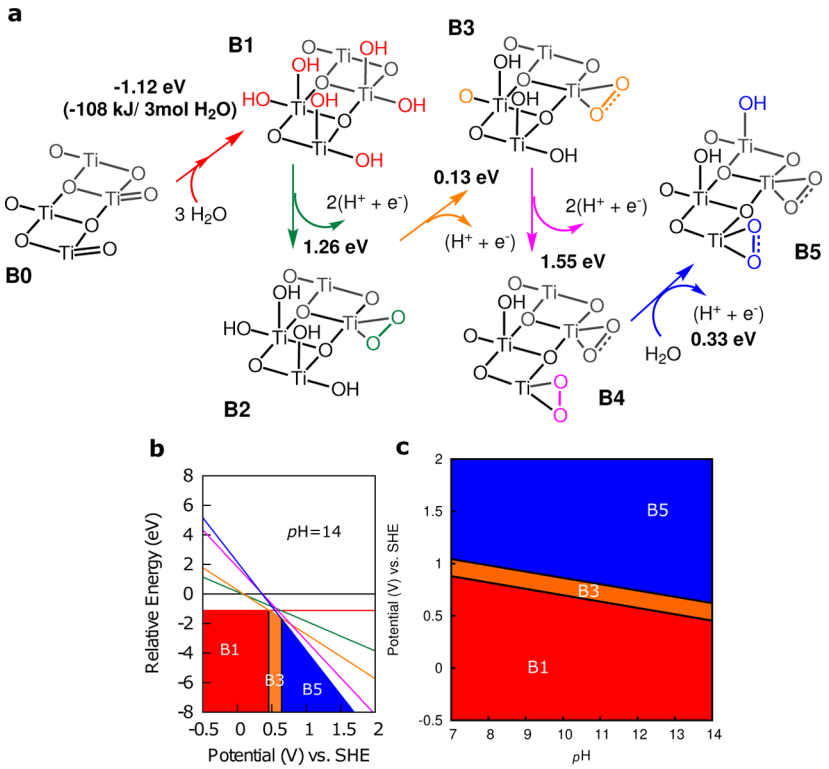

Figure 3. (a) Reverse Latimer (hydration and oxidation) diagram for the 2 × 1 TiO_2-DL surface. The diagram shows a series of hydration and deprotonation reactions leading to O-enrichment of the reconstructed surface. It shows the transformation of the adsorbate-free surface (B0) into the most oxidized form of the surface (B5), passing through the most stable intermediates (B1, B2, B3, and B4). A single bond between two O atoms indicates a peroxo, while a one-and-a-half bond indicates a superoxo species. The schematics show only the top basis atoms of the 2 × 2 supercell (simulation size). The species experiencing chemical changes are in color. The Gibbs free energies of the reactions are indicated next to the arrows (vs SHE, pH = 14). B4 and B5 are R3 and R4 of Figure 4b, respectively. The corresponding relative surface free energy at pH = 14 as a function of applied potential (B0 + 4 H_2O is chosen as the zero energy) and the Pourbaix diagram are shown in (b) and (c), respectively.

and ε_{eq} are the equilibrium reduction potential of step i and of the overall reaction relative to a suitable reference, respectively. Here we use the standard hydrogen electrode as the reference. We can define the minimum η at which all $[U - \varepsilon(i)]$ are ≥ 0 to favor oxidation, which is $\eta_{min} = \max[\varepsilon(i) - \varepsilon_{eq}] = \Delta\varepsilon_{max}$. Note that the Gibbs free energy of step i oxidation half-reaction, $\Delta G_{ox}(i)$, (in eV) is equal to $e{\cdot}\varepsilon(i)$, where e is the electron charge.

A criterion for a good oxygen evolving catalyst, therefore, is having the maximum $\varepsilon(i)$ close to the reversible potential of the O_2/H_2O half reaction, (ε_{eq}; 1.23, 0.40 V vs standard hydrogen electrode at pH = 1, 14). This method has been shown to accurately capture experimental oxygen evolving activity trends of many inorganic metal oxides, metals, and biological cofactors containing metal oxides.[40−45] Thus, comparing $\Delta\varepsilon_{max}$ for different catalysts calculated by the same method is an excellent predictor of relative catalytic performance of oxides. Indeed oxides with exceptional oxygen evolving activity have low predicted $\Delta\varepsilon_{max}$.[39,42−45] See Materials and Methods section for details.

The use of thermodynamic and electronic property-based descriptors, either experimentally or theoretically determined, has gained popularity in the field because of their success in relating and predicting the kinetic behavior of transition-metal oxides toward water splitting.[6,13,46−49]

2.3. Surface Hydration and Oxidation. Prior to the theoretical activity study described above, the transformation of the surfaces in aqueous and oxidizing conditions must be evaluated. This is to determine the most thermodynamically favorable form of the surfaces that would perform the catalytic reactions. The hydration chemistry of the TiO_2 (001) termination of $SrTiO_3$ is very well studied.[50−53] While numerous literature for bulk-like termini are available, study on the water chemistry of surface reconstructions of $SrTiO_3$ is still emerging. Recent notable works in this field explores the hydration behavior[54,55] of the more reactive reconstructed (110) surface,[56] while another provides DFT-based partial hydration studies on the TiO_2-rich 2 × 1 (001) reconstruction.[28,29] In the later work, hydration was found to present a potential explanation for the ubiquity of the 2 × 1 reconstruction over the chemically related $c(2 \times 2)$ variant, attesting to the propensity of the former toward hydration to acquire seemingly anomalous stability.[28,29]

DFT-based studies on the water oxidation path for O_2 synthesis on perovskite oxides has also been well documented. However, in these studies, the bulk-like termini, for example, the TiO_2 (001) for Ti-based perovskites, were the only surfaces considered.[45]

The stability of the 1 × 1 TiO_2 (denoted as A0 in Figure S7 in the Supporting Information) and 2 × 1-DL (denoted as B0 in Figure S8 in the Supporting Information and Figure 3) with respect to their hydrated and more oxidized forms were determined. This is done considering operational electrochemical conditions (298 K, equilibrium with an aqueous environment, pH = 14, and subjected to an anodic (oxidizing) potential). To find the most stable surfaces in these conditions, H_2O molecules have been added to both A0 and B0, and then H atoms have been progressively removed from them. This is

DOI: 10.1021/ja511332y
J. Am. Chem. Soc. 2015, 137, 2939−2947

because it is expected that the surface becomes more O-rich as the potential bias becomes increasingly anodic. The complete hydration and oxidation diagrams are constructed for the bulk-like TiO_2 and the 2 × 1-DL surfaces and are shown in Figures S7 and S8 in the Supporting Information, respectively. Figure 3a shows the most stable path to hydration and oxidation (reverse Latimer diagram) for the 2 × 1-DL surface (2 × 2 surface cell). Starting from the pristine 2 × 1-DL (B0), the surface is hydrated, preferentially on the ^{a}Ti sites first then on a ^{b}Ti site, leading to B1 (net hydration process is the red path). From this hydrated form, oxidation occurs by taking out electrons with the release of protons from the surface hydroxyls: total of $2(H^+ + e^-)$ leading to B2 (green path), $3(H^+ + e^-)$ leading to B3 (yellow), $5(H^+ + e^-)$ leading to B4 (pink), and finally, $6(H^+ + e^-)$ with the addition of water leading to B5 (blue). The oxidized structures feature side-on coordinated O_2 (η^2–O_2) molecules that are linked to the ^{a}Ti atoms, either horizontally or vertically oriented, while hydroxide ions are adsorbed on the ^{a}Ti and ^{b}Ti atoms. These surface η^2–O_2 exhibit either peroxo (single bond) or superoxo (one-and-a-half bond) characteristics as demonstrated by their charges, bond-lengths, and vibrational frequencies, as shown in Table 1. Shown in Figure 1f,g is the highly oxidized form of the 2 × 1-DL reconstruction (B5).

Table 1. Calculated Löwdin charges, Bond Lengths, And Stretching Frequencies of the O_2 Moieties in the Structures in the Catalytic Cycle of the Reconstructed Surfaces[a]

structure	orientation	charge (e/molecule)	bond length (Å)	stretching ν (cm^{-1})
B2	horizontal	−0.75	1.40	971
B3	horizontal	−0.35	1.29	1174
R1	horizontal	−0.32	1.29	1173
R2	horizontal	−0.34	1.29	1173
R3 (B4)	horizontal	−0.72	1.41	961
	vertical	−0.36	1.30	1133
R4 (B5)	horizontal	−0.37	1.30	1156
	vertical	−0.33	1.29	1179
bulk O[b]		−1.05		
H_2O_2 (g)[c]			1.475	877
$^{16}O_2^{\bullet-}$[c]			1.35	1090

[a]Structures are shown in Figure 3 and in the catalytic cycle in Figure 4b. The high- and low-charge species show the lengths and vibrational frequencies of peroxo and superoxo ligands.[57] [b]Bulk lattice O charge is shown for comparison. [c]Experimental constants taken from NIST chemistry WebBook.[58]

The relative stability of the hydrated and oxidized surfaces vary with the applied potential and pH as shown in Figure 3b,c. The Gibbs free energies, ΔG_{ox}, therein (in eV) for conversion of surface XN to XN' are calculated using

$$\Delta G_{ox} = \Delta G^\circ_{SHE} + \Delta G^\circ_{ox} - n{\cdot}e{\cdot}U - n{\cdot}0.0592{\cdot}pH \quad (1)$$

where ΔG°_{SHE} = 0 eV is the Gibbs free energy change of the SHE, which serves as the reference, ΔG°_{ox} is the standard Gibbs free energy change of the oxidation reaction:

$$XN + mH_2O(l) \rightarrow XN' + n(H^+ + e^-) + rO_2$$

calculated using energies from DFT simulation and gas-phase experimental entropies.[58] U is the applied potential against the SHE, and e is the electron charge. See the"Additional Computational Methods" section in Supporting Information for the details of the calculations of ΔG°_{ox}.

Figure 3b shows that the surface undergoes spontaneous hydration to B1 (red region), and then is subsequently oxidized at 0.46 V (= [1.26 + 0.13]eV/3e^-) to B3 (orange region). At 0.63 V (= [1.55 + 0.33]eV/3e^-), the surface is further oxidized to B5 (blue region). Figure 3c shows the corresponding Pourbaix diagram from pH = 7 to 14. It illustrates how the coexistence potential varies with pH. The water splitting chemistry is done in excess of the equilibrium potential (0.40 V at pH = 14), and each individual elementary step requires much larger potential to be spontaneous, as shown later. And thus, at these realistic kinetically permissive potentials (≫0.4 V), the most relevant surface would be B5.

2.4. Catalytic Mechanism. The O_2 evolution catalytic cycles on the relevant highly oxidized bulk-like TiO_2 (A3 in Figure S7, or L3) and 2 × 1-DL surfaces (B5 or R4) are shown in Figure 4a,b, respectively. We first discuss the chemical details of their respective elementary steps, then we proceed to

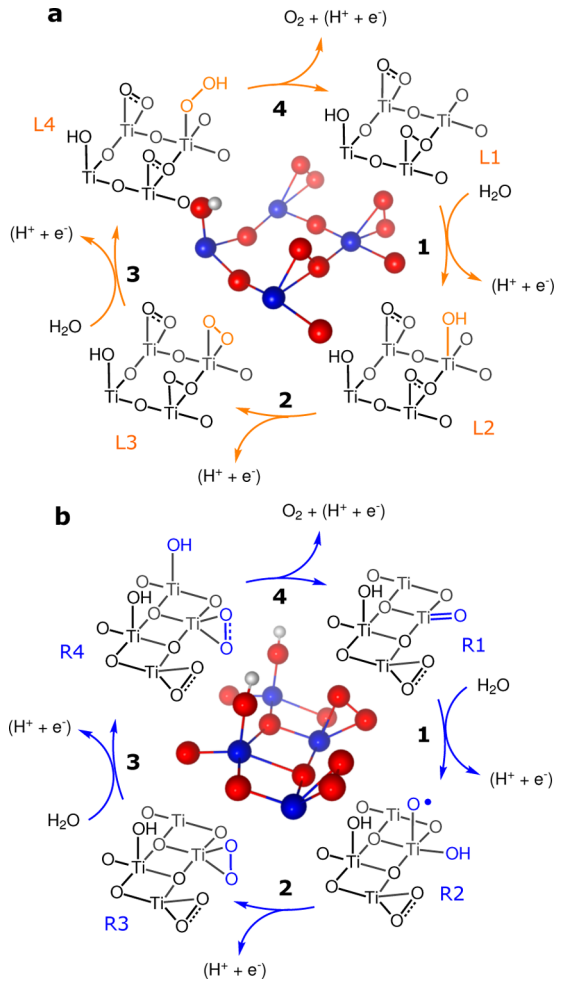

Figure 4. (a) Oxygen evolving reaction cycle on the bulk-like TiO_2 termination and (b) on the 2 × 1-DL reconstruction. A single bond between two O atoms indicates a peroxo, while a one-and-a-half bond indicates a superoxo species. Schematics show only the basis units of the top TiO_2 layer of the 2 × 2 supercells (simulation size). For a complete cycle, two water molecules are consumed, and an O_2 molecule and 4 H^+ ions are produced. The species experiencing chemical changes are in color. See Table 2 for the required applied potential for each reaction step to be driven to spontaneity.

DOI: 10.1021/ja511332y
J. Am. Chem. Soc. 2015, 137, 2939–2947

comparing and contrasting the two, both qualitatively and quantitatively. Single-site activity study is performed to be able to simulate a low-frequency reaction (only a small fraction of the sites undergo O_2 formation at one time), and thus the neighbor of the "active site" is likely fixed to the equilibrium configuration during the reaction. The 2 × 2 simulation size is the smallest cell in which this can be modeled. Thus, while the neighbor is transiently"inactive", this site is able to participate in the chemical reaction as well.

The oxidation cycle on the bulk-like TiO_2 termination is shown in Figure 4a. The mechanistic study is similar to the one presented in ref 45. Figure 4a shows the likely reaction cycle operative at potentials between 0.50 and 1.5 V. Reaction step (1) produces a OH on a Ti site, followed by (2), production of O directly coordinated to a lattice O. The coordination of the O adatom to a lattice O removes the necessity to oxidize the Ti site further where instead a surface peroxide O_2^{2-} is formed. Since the lattice O are already bound to two Ti atoms, they have to expand their valence to three to be available to accommodate the extra O. (3), OOH may then form upon another oxidative attack by water on the same site, and (4), finally releases an O_2, freeing the Ti site available to undergo another cycle.

O_2 evolution on the 2 × 1-DL surface, on the other hand, is achieved as follows (shown in Figure 4b): (1) Beginning with surface R1, ^{a}Ti═^{a}O is oxidized by adding H_2O and losing a proton, resulting in an O radical. (2) Further oxidation of the ^{a}Ti site generates a peroxo-type O_2 ligand (see diatomic parameters in Table 1). (3) After another single electron oxidation at the ^{a}Ti site, coupled with the adsorption of a hydroxo at the ^{b}Ti site, the R4 (B5) structure (Figure 1g) is generated. The O_2 bond contracts, its stretching frequency rises, and the Löwdin charge decreases, consistent with forming a superoxo (Table 1). These changes are accompanied by the removal of a proton from a water molecule at the ^{b}Ti site, as summarized by the reactions in Scheme 1. (4) Finally,

Scheme 1. Proton-Coupled Electron-Transfer Step Involving both ^{a}Ti and ^{b}Ti Simultaneously in Step 3 of Figure 4b

$$^aTi(\eta^2\text{-}O_2) \longrightarrow {}^aTi(\eta^2\text{-}O_2)^+ + e^-$$

$$^bTi + H_2O \longrightarrow {}^bTi(OH)^- + H^+$$

deprotonation at the ^{b}Ti site creates an O^{2-} that replaces the desorbed dioxygen molecule at the ^{a}Ti, regenerating R1. This step is suggested by our DFT relaxation studies; when an O atom is on the ^{b}Ti site and an O_2 is present on the ^{a}Ti site, the O_2 spontaneously desorbs.

Projected density of states (PDOS) calculations show that the states near the Fermi level are mostly derived from adsorbate O/O_2 frontier orbitals (Figure 5). Completely filled and partially empty O−2p states on R1 and R2, respectively, fully filled O_2^{2-}−π*orbitals on R3, and a half-filled O_2^-−π*orbital on R4 confirm the transformation from oxo, to oxo radical, to peroxo, and finally, to superoxo after steps (1), (2), and (3), respectively.

There are two distinct features in the mechanism proposed here that are often not explicitly touched on in other proposed mechanisms for O_2 production from water on oxides. First, our mechanism is of the Mars−van Krevelen-type,[59] but with H_2O as the O source. A lattice oxygen (^{a}O) participates directly as a reactant, which is then replenished by a fully deprotonated

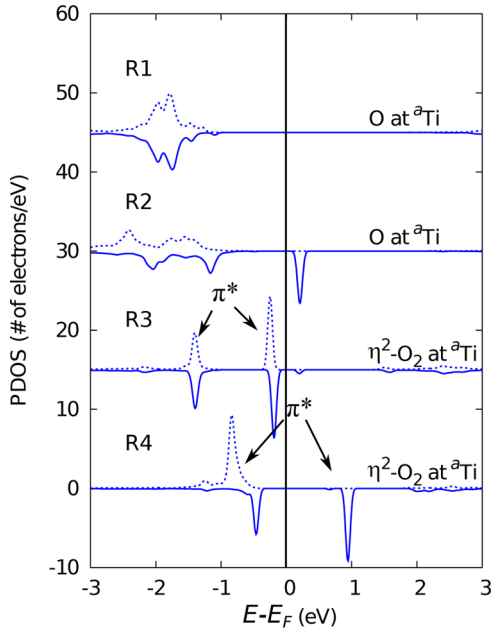

Figure 5. Atomic orbital (2s and 2p states) PDOS of the O species in the catalytic cycle for the 2 × 1 TiO_2-DL surface in Figure 4b. Broken line: majority spin states, solid line: minority spin states. E_F is the Fermi level, where states are occupied and unoccupied below and above this line, respectively. The orbital occupation is consistent with oxo, oxo radical, peroxo, and superoxo orbital occupation schemes, from top to bottom. The splitting of the O_2−π* orbitals is due to the sigma bonding interaction interaction of one of these orbitals with ^{a}Ti.

water. Mars−van Krevelen-type mechanisms often operate in catalytic oxidation reactions, but the lattice O is usually replenished through dissociative adsorption of O_2. Second, there are two types of active metal sites on the surface, different in the way they share electrons with their adsorbates, i.e., one is nucleophilic, the more electron-rich: ^{a}Ti, while the other is electrophilic, ^{b}Ti. Usually, the mechanism involving transition-metal oxides assumes that all active metal sites are homogeneous. In our mechanism, the two types of Ti on the surface have a synergistic effect on the O_2 production process. ^{a}Ti serves as excellent binding site for electrophilic radicals such as $^\bullet$OH and $^\bullet$O$^\bullet$, where they undergo a redox reaction with the ^{a}Ti═^{a}O. The presence of a nucleophile, such as OH^- and O^{2-}, on ^{b}Ti then makes it easier to oxidize O_2^{2-}/O_2^- on ^{a}Ti, which leads to the production of O_2. Thus, together they perform as one nearly ideal catalytic unit. Another defining characteristic of the mechanism is that the positive charge is accumulated on the O species and not on the Ti; the Ti charges remain at +4 throughout the cycle.

The difference between the mechanism on the 1 × 1 and on the 2 × 1-DL is that in the 1 × 1, the lattice O is strongly bound to the surface such that an oxygen vacancy would be required to form between two Ti atoms if the lattice O is to participate in the O_2 generation. Therefore, in the former case, O_2 is produced from incoming water molecules exclusively. This is unlike the singly coordinated ^{a}O found on the 2 × 1 reconstructed surface. Also, the Ti atoms in the former case are essentially catalytically independent. We note that each Ti in the unreconstructed surface is connected to another by only one O bridging atom and are at least 4 Å away from each other. In the 2 × 1, the Ti ions (^{a}Ti and ^{b}Ti) are connected by two bridging O atoms and are only ≈2.8 Å away from each other.

DOI: 10.1021/ja511332y
J. Am. Chem. Soc. 2015, 137, 2939−2947

Table 2 shows the calculated potential bias, U vs SHE, required to make each step in the mechanisms shown in Figure

Table 2. Minimum Required Applied Potentials, U (vs SHE), at pH =14 Predicted to Make the Elementary Steps of the Catalytic Cycles Spontaneous[a]

	potential (V)	
step	(1 × 1)TiO_2	(2 × 1)TiO_2-DL
1	0.25	0.92
2	1.45	0.05
3	0.44	0.33
4	−0.53	0.30

[a]The catalytic cycles are shown in Figure 4.

4 reversible at pH = 14. The largest biases are 1.45 V ($\Delta\varepsilon_{max}$ = 1.05 V) and 0.92 V ($\Delta\varepsilon_{max}$ = 0.52 V) for the bulk-like TiO_2 and the 2 × 1-DL reconstruction, respectively. The overpotential ($\Delta\varepsilon_{max}$) lowering found in the 2 × 1-DL reconstruction agrees with the experimentally found increase in its catalytic activity. Although it is difficult to quantitatively ascribe the 0.5 V reduction in the theoretical thermodynamic overpotential, $\Delta\varepsilon_{max}$, to any of the Tafel parameters, this lowering is believed to corresponds to barrier reduction in the rate-limiting step leading to an enhanced rate.[39,42−45] This could potentially explain the difference between the oxygen evolution rates experimentally found for the two surfaces.

Comparable DFT evaluations of the overpotential for water splitting on the (110) terminated rutile-type oxides (RuO_2, IrO_2, and TiO_2)[43,44] and (100) terminated perovskite-type oxides[45] have been reported. In these studies, the barriers to forming OH, O, OOH, and O_2 as assisted by those oxide surfaces have been calculated (employing the same mechanism presented for the 1 × 1 TiO_2 surface discussed above). These studies found an overpotential trend that is consistent with the experimental overpotential trends (for example, for rutile-type oxides the overpotential trend is TiO_2 > IrO_2 > RuO_2).[43,45] A 0.37 V thermodynamic overpotential was found for RuO_2, 0.56 V for IrO_2,[43] and a higher overpotential for TiO_2, 0.78 V.[44] Clearly, the diverse coordination on the reconstructed surface of $SrTiO_3$ are an improvement over those (110) termination of the rutile-type TiO_2 and (001) TiO_2-termination of $SrTiO_3$. This further illustrates that the cubane-like structure of the 2 × 1-DL, which is not present on either the rutile (110) surface or the bulk-like TiO_2 termination of $SrTiO_3$, is the key component in the reconstruction's reactivity.

2.5. Comparison with Biological and Molecular Systems. A mechanism involving two active sites is a common theme in known efficient water-splitting molecular and biological catalysts. For example, in the Mn_4CaO_5 cluster found in the oxygen evolving center (OEC) of the photosystem II protein complex,[60,61] a highly electron-deficient O species is produced on the terminal Mn not belonging to the Mn_3CaO_4 cube, while the Ca^{2+} acts as binding site for nucleophilic OH^-/H_2O. Together these species react to form O_2, either via a nucleophilic attack on the electrophilic oxo group on the Mn site or oxyl radical attack on the adsorbed water on Ca.[60−64] A mechanism requiring dual active site has been proposed for some dinuclear Ru-based molecular water-oxidation catalysts as well.[64,65] The two strongly electronically coupled Ru sites perform distinct roles, where only one Ru supports and produces the O_2.[64,65]

Here, the role of site complementary on the reconstructed surface of $SrTiO_3$ has been shown to be of significance, where two sites that bind and make available electron-deficient and electron-rich O species are in tandem. Such are the roles of the two electronically distinct Ti sites in the reconstruction. This design principle, suggested to be beneficial for molecular and biological systems, seems to be universal and could also be a strong concept to adopt in heterogeneous catalysts, as theoretically demonstrated herein.

3. MATERIALS AND METHODS

3.1. Surface Synthesis and Characterization. To obtain the 2 × 1 surface we process the as received single crystals (0.7% Nb w/w or 1.4 mol %, MTI Corp.) as follows: (1) UHV outgassing at 600 °C for 30 min; (2) UHV Sputter with Ar^+ for 10 min at 1 kV and 1.1 μA ion current, followed by UHV (2 × 10^{-10} Torr) annealing at 600 °C for 20 min, this sputter−anneal cycle is performed twice; (3) ultrasonication in water bath[20] at room temp for 1 h in air; (4) etch for 90 s in a commercial buffered hydrofluoric acid etchant[26,66] (NH_4F:HF = 6:1 by volume) in air, rinse with water and dry with N_2 stream; (5) furnace treatment at 980 °C for 2 h with 5 °C/min ramp rate[22] and O_2 flow (ultra high purity) at 2.5 L/min; (6) UHV anneal at 1020 °C for 10 min or more as needed to obtain sharp and intense 2 × 1 surface reconstruction measured by LEED. After electrolysis we confirm with LEED the 2 × 1 reconstruction by UHV annealing at ≈950 °C for ≈6−7 min. Control samples were generated using incomplete combinations of these processes, namely, as received, etched = (3) + (4), sputteranneal + furnace = (1) + (2) + (5), sputteranneal + etched + furnace = (1) + (2) + (3) + (4) + (5), and UHV = (6) for 10 min. LEED images were obtained at 38, 48, 61, 76, and 98 eV. 38 eV was found to be most suitable to get sharp 2 × 1 patterns. The samples were radiatively heated, and temperatures were measured using an optical pyrometer.

3.2. Electrode Preparation and Photoelectrochemical Measurements. The (2.5 or 5) × 5 × 0.5 mm^3 sized crystals were painted with Ga−In eutectic (99.99%) on the unpolished side to serve as the ohmic contact. Copper wires were then attached to this side of the crystals using Ag paint. Heat-shrink tubes were used to insulate the entire lengths of the Cu wires, while waterproof epoxy was used to insulate the back of the crystals (Figure S11 in the Supporting Information). A three-electrode setup was constructed, and a custom-built glass photoelectrochemical cell equipped with a quartz window was used for all electrochemical measurements, shown in Figure S12 in the Supporting Information. The Epsilon Electrochemical workstation from BASi Analytical instruments was used as the potentiostat. A 23 cm Pt coil was used as the auxiliary electrode, while a single-junction Ag/AgCl electrode (in 4 M KCl electrolyte saturated with AgCl, Fisher Scientific Accumet) was used as the reference (+0.20 V vs SHE). Prior to electrochemical measurements, the sample electrode is soaked in 1 M NaOH for ≈1 h. Electrochemical measurements were recorded in 1 M NaOH aqueous solution, with and without UV−vis light illumination from a 200 W Hg(Xe) lamp. The I−V and I−t curves were measured with acquisition frequencies of 1/10 and 0.1 Hz, respectively.

3.3. Resistivity and Optical Properties. The resistivities of the samples were measured via the four-point probe method using a Cascade Microtech prober with 1.25 mm probe spacings. Using a J. A. Woollam M-2000 ellipsometer, dielectric properties, n and k, were extracted from raw data using an empirical spline fit. Reflectivities were taken at 65° angle averaged over different light polarizations.

3.4. Theoretical Calculations. DFT calculations were performed with the Perdew−Burke−Ernzerhof (PBE)[67] generalized gradient approximation (GGA) for the exchange−correlation functional as implemented in the Quantum Espresso (QE) package.[68] The effect of applying an effective Hubbard-U correction[69] onto the Ti 3d orbitals on the reaction energies in the catalytic cycles was checked and is shown in Figure S13 in the Supporting Information. The effective U was determined to be 4.72 eV from a linear-response calculation[69] involving a 2 × 2 × 2 $SrTiO_3$ supercell. Norm-conserving optimized

DOI: 10.1021/ja511332y
J. Am. Chem. Soc. 2015, 137, 2939−2947

designed nonlocal pseudopotentials[70−72] were generated using the OPIUM package.[73] Four-unit-cell-thick slabs with 2 × 2 surface supercells and in-plane lattice constant of 3.95 Å were used to simulate the surfaces. A vacuum separation of ≈16 Å in the direction normal to the slab has been included, with a dipole correction[74] in the same direction to eliminate artificial electrostatic interactions. The Brillouin zone was sampled via the Monkhorst−Pack[75] method with a 3 × 3 × 1 mesh. As for the molecules (H_2 and H_2O), the total energy of a gas-phase molecule was approximated by calculating the energy of an isolated molecule that is separated from its repeat image by 12 Å along three orthogonal directions. In the H_2O case, a dipole correction was also employed along the direction of the molecule's dipole. We performed spin-unrestricted calculations when deemed necessary. Structural relaxation has been carried out until the force on each atom is below 0.01 eV/Å. We calculated the Gibbs free energies of the reactions using the DFT energies (T = 0 K) and extrapolated to 298 K using the experimental entropies[58] of the gas-phase reactants and products. Zero point energy corrections to the total energy were calculated, applying the harmonic approximation, using linear response Γ-point phonon calculations for the surfaces and molecules as implemented in the QE package (see "Additional Computational Methods" section in the Supporting Information). For the surface phonon calculations, only motions of the TiO_2 overlayer or the top bulk-like layer were considered. This was done because we assume that the zero point energy contributions of the bottom layers would simply cancel each other out in the Gibbs free energy change calculations.

We used the electrochemical oxide path proposed by J. O. Bockris[47,76] as the initial guess for the mechanism. We then introduced modifications in the reaction mechanism and intermediate states guided by the results in the DFT relaxation studies. The slabs remain insulating even in the presence of adsorbates, indicating that there is no significant long-range electronic reorganization among different sites on the surface or in the bulk to accommodate the adsorbates.

See "Additional Computational Methods" in the Supporting Information for the thermodynamic framework of the catalytic efficiency analysis.

■ ASSOCIATED CONTENT

Supporting Information

Additional LEED, $I-V$ and $I-t$ curves, resistivity and optical measurements, tabulated Tafel parameters, diagrams of the experimental setup, extended computational methods, other DFT-predicted thermodynamic diagrams, additional catalytic cycles, and tabulated hydration and oxidation free energies of the surfaces. Structure cif files of all the relevant structures. This material is available free of charge via the Internet at http://pubs.acs.org.

■ AUTHOR INFORMATION

Corresponding Author

*rappe@sas.upenn.edu

Notes

The authors declare no competing financial interest.

■ ACKNOWLEDGMENTS

J.M.P.M. acknowledges the support from the Office of Naval Research under grant N00014-14-1-0761. S.K. was supported by US DOE through grant no. DE-FG02-07ER15920. A.M.R. acknowledges support of the Air Force Office of Scientific Research through grant number FA9550-10-1-0248. Computational support was provided by HPCMO of US DoD and NERSC. E.H.M., D.A.B., M.C., and T.R.G. would like to acknowledge the support by the Nano Bio Interface Center (NBIC), National Science Foundation Grant NSEC DMR-0832802. B.T.D. was supported by the US DOE, Office of Basic Energy Sciences, Materials Sciences and Engineering Division, award no. DE-SC0002158. C.B.M. is grateful for the support of the Richard Perry University Professorship. VESTA was used for the 3D structural models throughout this paper (ref 77).

■ REFERENCES

(1) Compton, R. G. *Comprehensive Chemical Kinetics*; Elsevier Science Publishing Company Inc.: Amsterdam, The Netherlands, 1987; Vol. *27*.

(2) Kanan, M. W.; Nocera, D. G. *Science* **2008**, *321*, 1072−5.

(3) Yang, H. G.; adh S. Z.Qiao, C. H. S.; Zou, J.; Liu, G.; Smith, S. C.; Cheng, H. M.; Lu, G. Q. *Nature* **2008**, *453*, 638.

(4) Esswein, A. J.; Surendranath, Y.; Reece, S. Y.; Nocera, D. G. *Energy Environ. Sci.* **2011**, *4*, 499.

(5) Hocking, R. K.; Brimblecombe, R.; Chang, L.-Y.; Singh, A.; Cheah, M. H.; Glover, C.; Casey, W. H.; Spiccia, L. *Nat. Chem.* **2011**, *3*, 461.

(6) Suntivich, J.; May, K. J.; Gasteiger, H. A.; Goodenough, J. B.; Shao-Horn, Y. *Science* **2011**, *334*, 1383−1385.

(7) Gardner, G. P.; Go, Y. B.; Robinson, D. M.; Smith, P. F.; Hadermann, J.; Abakumov, A.; Greenblatt, M.; Dismukes, G. C. *Angew. Chem., Int. Ed.* **2012**, *51*, 1616−1619.

(8) Bediako, D. K.; Lassalle-Kaiser, B.; Surendranath, Y.; Yano, J.; Yachandra, V. K.; Nocera, D. G. *J. Am. Chem. Soc.* **2012**, *134*, 6801−6809.

(9) Robinson, D. M.; Go, Y. B.; Mui, M.; Gardner, G.; Zhang, Z.; Mastrogiovanni, D.; Garfunkel, E.; Li, J.; Greenblatt, M.; Dismukes, G. C. J. *Am. Chem. Soc.* **2013**, *135*, 3494−3501.

(10) Wrighton, M. S.; Ellis, A. B.; Wolczanski, P. T.; Morse, D. L.; Abrahamson, H. B.; Ginley, D. S. J. *Am. Chem. Soc.* **1976**, *98*, 2774−2779.

(11) Bolts, J. M.; Wrighton, M. S. J. *Phys. Chem.* **1976**, *80*, 2641−2645.

(12) Bocarsly, A. B.; Bolts, J. M.; Cummins, P. G.; Wrighton, M. S. *Appl. Phys. Lett.* **1977**, *31*, 568.

(13) Betley, T. A.; Wu, Q.; Van Voorhis, T.; Nocera, D. G. *Inorg. Chem.* **2008**, *47*, 1849−61.

(14) Matsumura, M.; Hiramoto, M.; Tsubomura, H. *J. Electrochem. Soc.* **1983**, *130*, 326.

(15) Kato, H.; Kudo, A. *J. Phys. Chem. B* **2002**, *106*, 5029−5034.

(16) Yin, J.; Ye, J.; Zou, Z. *Appl. Phys. Lett.* **2004**, *85*, 689.

(17) Konta, R.; Ishii, T.; Kato, H.; Kudo, A. *J. Phys. Chem. B* **2004**, *108*, 8992−8995.

(18) Maegli, A.; Yoon, S.; Otal, E.; Karvonen, L.; Mandaliev, P.; Weidenkaff, A. *J. Solid State Chem.* **2011**, *184*, 929−936.

(19) Jiang, Q.; Zegenhagen, J. *Surf. Sci.* **1999**, *425*, 343−354.

(20) Koster, G.; Kropman, B. L.; Rijnders, G. J. H. M.; Blank, D. H. A.; Rogalla, H. *Appl. Phys. Lett.* **1998**, *73*, 2920.

(21) Castell, M. R. *Surf. Sci.* **2002**, *505*, 1−13.

(22) Erdman, N.; Poeppelmeier, K. R.; Asta, M.; Warschkow, O.; Ellis, D. E.; Marks, L. D. *Nature* **2002**, *419*, 55−8.

(23) Erdman, N.; Marks, L. *Surf. Sci.* **2003**, *526*, 107−114.

(24) Erdman, N.; Warschkow, O.; Asta, M.; Peoppelmeier, K. R.; Ellis, D. E.; Marks, L. D. *J. Am. Chem. Soc.* **2003**, *125*, 10050.

(25) Lanier, C. H.; van der Walle, A.; Erdman, N.; Landree, E.; Warschkow, O.; Kazimirov, A.; Poeppelmeier, K. R.; Zegenhagen, J.; Asta, M.; Marks, L. D. *Phys. Rev. B* **2007**, *76*, 045421.

(26) Bachelet, R.; Sanchez, F.; Palomares, F. J.; Ocal, C.; Fontcuberta, J. *Appl. Phys. Lett.* **2009**, *95*, 141915.

(27) Kienzle, D. M.; Becerra-Toledo, A. E.; Marks, L. D. *Phys. Rev. Lett.* **2011**, *106*, 176102−1−4.

(28) Becerra-Toledo, A.; Castell, M.; Marks, L. *Surf. Sci.* **2012**, *606*, 762−765.

(29) Becerra-Toledo, A.; Enterkin, J.; Kienzle, D.; Marks, L. *Surf. Sci.* **2012**, *606*, 791−802.

(30) Zhu, G.-z.; Radtke, G.; Botton, G. A. *Nature* **2012**, *490*, 384−387.

(31) Wu, C.; Kruska, K.; Castell, M. R. *Surf. Sci.* **2013**, *618*, 94−100.

DOI: 10.1021/ja511332y
J. Am. Chem. Soc. 2015, 137, 2939−2947

(32) Gerhold, S.; Wang, Z.; Schmid, M.; Diebold, U. *Surf. Sci.* **2014**, *621*, L1−L4.
(33) Heifets, E.; Piskunov, S.; Kotomin, E. A.; Zhukovskii, Y. F.; Ellis, D. E. *Phys. Rev. B* **2007**, *75*, 115417−1−13.
(34) Herger, R.; Willmott, P.; Bunk, O.; Schleptz, C.; Patterson, B.; Delley, B. *Phys. Rev. Lett.* **2007**, *98*, 076102.
(35) Herger, R.; Willmott, P.; Bunk, O.; Schleptz, C.; Patterson, B.; Delley, B.; Shneerson, V.; Lyman, P.; Saldin, D. *Phys. Rev. B* **2007**, *76*, 195435.
(36) Matsuda, T.; Yoshida, Y.; Mitsuhara, K.; Kido, Y. *J. Chem. Phys.* **2013**, *138*, 244705.
(37) Rieger, P. H. *Electrochemistry*; 2nd ed.; Chapman & Hall: New York,1994.
(38) Lin, Y.; Wen, J.; Hu, L.; McCarthy, J. A.; Wang, S.; Poeppelmeier, K. R.; Marks, L. D. *Micron* **2015**, *68*, 152−157.
(39) Nørskov, J. K.; Rossmeisl, J.; Logadottir, A.; Lindqvist, L.; Kitchin, J. R.; Bligaard, T.; Jònsson, H. *J. Phys. Chem. B* **2004**, *108*, 17886−17892.
(40) Rossmeisl, J.; Logadottir, A.; Nørskov, J. K. *Chem. Phys.* **2005**, *319*, 178−184.
(41) Rossmeisl, J.; Nørskov, J. K.; Taylor, C. D.; Janik, M. J.; Neurock, M. *J. Phys. Chem. B* **2006**, *110*, 21833−21839.
(42) Rossmeisl, J.; Dimitrievski, K.; Siegbahn, P.; Nørskov, J. K. *J. Phys. Chem. C* **2007**, *111*, 18821−18823.
(43) Rossmeisl, J.; Qu, Z. W.; Zhu, H.; Kroes, G. J.; Nørskov, J. K. *J. Electroanal. Chem.* **2007**, *607*, 83−89.
(44) Valdés, A.; Qu, Z.-W.; Kroes, G.-J.; Rossmeisl, J.; Nørskov, J. K. *J. Phys. Chem. C* **2008**, *112*, 9872−9879.
(45) Man, I. C.; Su, H.-Y.; Calle-Vallejo, F.; Hansen, H. A.; Martínez, J. I.; Inoglu, N. G.; Kitchin, J.; Jaramillo, T. F.; Nørskov, J. K.; Rossmeisl, J. *ChemCatChem* **2011**, *3*, 1159−1165.
(46) Bockris, J. O.; Otagawa, T. *J. Electrochem. Soc.* **1984**, *131*, 290−302.
(47) Matsumoto, Y.; Sato, E. *Mater. Chem. Phys.* **1986**, *14*, 397−426.
(48) Vojvodic, A.; Nørskov, J. K. *Science* **2011**, *334*, 1355−1356.
(49) Koper, M. T. M. *J. Electroanal. Chem.* **2011**, *660*, 254−260.
(50) Evarestov, R.; Bandura, A.; Alexandrov, V. *Surf. Sci.* **2007**, *601*, 18441856.
(51) Baniecki, J. D.; Ishii, M.; Kurihara, K.; Yamanaka, K.; Yano, T.; Shinozaki, K.; Imada, T.; Kobayashi, Y. *J. Appl. Phys.* **2009**, *106*, 054109.
(52) Guhl, H.; Miller, W.; Reuter, K. *Phys. Rev. B* **2010**, *81*, 155455.
(53) Hussain, H.; Torrelles, X.; Rajput, P.; Nicotra, M.; Thornton, G.; Zegenhagen, J. *J. Phys. Chem. C* **2014**, *118*, 10980−10988.
(54) Wang, Z.; Hao, X.; Gerhold, S.; Novotny, Z.; Franchini, C.; McDermott, E.; Schulte, K.; Schmid, M.; Diebold, U. *Phys. Chem. C* **2013**, *117*, 26060−26069.
(55) Li, W.; Liu, S.; Wang, S.; Guo, Q.; Guo, J. *J. Phys. Chem. C* **2014**, *118*, 2469−2474.
(56) Enterkin, J. A.; Subramanian, A. K.; Russell, B. C.; Castell, M. R.; Poeppelmeier, K. R.; Marks, L. D. *Nat. Mater.* **2010**, *9*, 245.
(57) Cramer, C.; Tolman, W.; Theopold, K.; Rheingold, A. *Proc. Natl. Acad. Sci. U. S. A* **2003**, *100*, 3635−3640.
(58) *NIST Chemistry WebBook*; http://webbook.nist.gov/chemistry/.
(59) Doornkamp, C.; Ponec, V. *J. Mol. Catal. A: Chem.* **2000**, *162*, 19−32.
(60) Ferreira, K. N.; Iverson, T. M.; Maghiaoui, K.; Barber, j.; Iwata, S. *Science* **2004**, *303*, 1831−1838.
(61) Umena, Y.; Kawakami, K.; Shen, J.-R.; Kamiya, N. *Nature* **2011**, *473*, 55−60.
(62) Dau, H.; Limberg, C.; Reier, T.; Risch, M.; Roggan, S.; Strasser, P. *ChemCatChem* **2010**, *2*, 724−761.
(63) Barber, J. *Chem. Soc. Rev.* **2009**, *38*, 185−196.
(64) Liu, F.; Concepcion, J. J.; Jurss, J. W.; Cardolaccia, T.; Templeton, J. L.; Meyer, T. J. *Inorg. Chem.* **2008**, *47*, 1727−1752.
(65) López, I.; Ertem, M. Z.; Maji, S.; Benet-Buchholz, J.; Keidel, A.; Kuhlmann, U.; Hildebrandt, P.; Cramer, C. J.; Batista, V. S.; Llobet, A. *Angew. Chem., Int. Ed.* **2014**, *53*, 205−209.
(66) Kawasaki, M.; Takahashi, K.; Maeda, T.; Tsuchiya, R.; Shinohara, M.; Ishiyama, O.; Yonezawa, T.; Yoshimoto, M.; Koinuma, H. *Science* **1994**, *266*, 1540−1542.
(67) Perdew, J. P.; Burke, K.; Ernzerhof, M. *Phys. Rev. Lett.* **1996**, *77*, 3865−8.
(68) Giannozzi, P.; et al. *J. Phys.: Condens. Matter* **2009**, *21*, 395502−20.
(69) Cococcioni, M.; de Gironcoli, S. *Phys. Rev. B* **2005**, *71*, 035105−1−16.
(70) Rappe, A. M.; Rabe, K. M.; Kaxiras, E.; Joannopoulos, J. D. *Phys. Rev. B* **1990**, *41*, 1227−30.
(71) Ramer, N. J.; Rappe, A. M. *Phys. Rev. B* **1999**, *59*, 12471−8.
(72) Grinberg, I.; Ramer, N. J.; Rappe, A. M. *Phys. Rev. B* **2001**, *63*, 201102(R)-1−4.
(73) *Opium - pseudopotential generation project*; http://opium.sourceforge.net.
(74) Bengtsson, L. *Phys. Rev. B* **1999**, *59*, 12301−4.
(75) Monkhorst, H. J.; Pack, J. D. *Phys. Rev. B* **1976**, *13*, 5188−5192.
(76) Bockris, J. O. *J. Chem. Phys.* **1956**, *24*, 817−827.
(77) Momma, K.; Izumi, F. *J. Appl. Crystallogr.* **2008**, *41*, 653−658.

DOI: 10.1021/ja511332y
J. Am. Chem. Soc. 2015, 137, 2939−2947